

See discussions, stats, and author profiles for this publication at: <https://www.researchgate.net/publication/231642101>

Conductance Bistability in a Single Porphyrin Molecule in a STM Junction: A Many-Body Simulation Study

ARTICLE *in* THE JOURNAL OF PHYSICAL CHEMISTRY C · JUNE 2007

Impact Factor: 4.77 · DOI: 10.1021/jp067586h

CITATIONS

8

READS

27

4 AUTHORS:



Jeremy B Maddox

Western Kentucky University

32 PUBLICATIONS 344 CITATIONS

SEE PROFILE



Upendra Harbola

Indian Institute of Science

54 PUBLICATIONS 979 CITATIONS

SEE PROFILE



Kenny Mayoral

University of California, Los Angeles

6 PUBLICATIONS 17 CITATIONS

SEE PROFILE



Shaul Mukamel

University of California, Irvine

852 PUBLICATIONS 23,680 CITATIONS

SEE PROFILE

Conductance Bistability in a Single Porphyrin Molecule in a STM Junction: A Many-Body Simulation Study

Jeremy B. Maddox,* Upendra Harbola, Kenny Mayoral, and Shaul Mukamel

Department of Chemistry, University of California, Irvine, California 92697-2025

Received: November 15, 2006; In Final Form: March 21, 2007

The conductance spectrum of the neutral and charged states of a single magnesium porphine molecule is simulated by calculating many-electron states at the Hartree–Fock and configuration interaction singles level; numerical results reproduce the hysteretic switching behavior observed in a recent experiment (Wu, S. W.; Ogawa, N.; Ho, W. *Science* **2006**, 312, 1362).

Introduction

Hysteretic switching in molecular junctions is an important factor for many applications of nanoscale electronic devices and has been demonstrated recently for carbon nanotubes¹ and a variety of oligophenylene-based compounds in both self-assembled monolayer assemblies² and single-molecule transistors.³ Other examples of molecular switching involve large conformational changes, such as those in cantenanes and rotoxanes,⁴ or isomerization of specific functional groups.⁵

Reversible switching of a single magnesium porphine (MgP) molecule adsorbed on an oxidized NiAl(110) surface in a scanning tunneling microscope (STM) junction was reported recently.⁶ This effect was attributed to charging and discharging events that could be detected by the retraction of the STM tip when the current was held constant and the bias voltage was scanned beyond some threshold. The oxide provides a secondary tunneling barrier between the molecule and substrate, on top of the tip-molecule vacuum barrier.⁷ This decouples the MgP from the NiAl(110) surface and is known to have a profound impact on STM measurements; vibronic transitions that are quenched entirely when the molecule is directly chemisorbed to a metallic surface can be resolved in both the STM conductance⁸ and current-induced single-molecule fluorescence spectra⁹ on the oxidized surface. Similar effects were observed in STM measurements on ultrathin porphyrin layers deposited on metal surfaces where the deeper organic layers act as the spacer, allowing the detection of the STM-induced emission signal.¹⁰ The alumina layer is expected to play a crucial role in the switching behavior of MgP since it is highly polarizable and can stabilize the charged molecular species, allowing an injected electron to be trapped on the molecule. The molecule–lead couplings may be much smaller than the charging energy, thus reducing the tunneling rates by Coulomb blockade.¹¹

Both electrostatic¹² and phonon-assisted¹³ mechanisms have been proposed to describe the switching behavior of molecular junctions. In the present work, we express the current through a STM junction in terms of many-electron molecular states with N and $N \pm 1$ electrons. We address differences between the conductance of the neutral and anionic charge states of MgP in terms of the voltage division across the STM junction and compare our numerical results with experiment.

Theoretical Approach

The STM junction consisting of a molecule (M) weakly coupled to a metallic tip (T) and a substrate (S) is displayed in Figure 1A. The total Hamiltonian is

$$H_{\text{total}} = H_{\text{M}} + H_{\text{T}} + H_{\text{S}} + W_{\text{T}} + W_{\text{S}} \quad (1)$$

where

$$H_{\text{M}} = \sum_{ij} t_{ij} \psi_i^\dagger \psi_j + \frac{1}{2} \sum_{ijkl} v_{ijkl} \psi_i^\dagger \psi_j^\dagger \psi_l \psi_k \quad (2)$$

is the many-electron Hamiltonian for the isolated molecule; t_{ij} and v_{ijkl} are the one-electron core and two-electron Coulomb matrix elements, respectively. The isolated tip and substrate are treated as noninteracting electron systems

$$H_{\text{X}} = \sum_{i \in \text{X}} \epsilon_i \psi_i^\dagger \psi_i \quad \text{X} = \text{T, S} \quad (3)$$

where H_{T} and H_{S} represent the isolated tip and substrate, respectively. The molecule–tip W_{T} and molecule–substrate coupling W_{S} are given by

$$W_{\text{X}} = \sum_{i \in \text{M}} \sum_{k \in \text{X}} V_{ik} \psi_i^\dagger \psi_k + V_{ki} \psi_k^\dagger \psi_i \quad \text{X} = \text{T, S} \quad (4)$$

The Fermi operators ψ_i^\dagger and ψ_i create and destroy, respectively, an electron in orbital ϕ_i with energy ϵ_i , and V_{ik} is the coupling between orbitals $\phi_{i \in \text{M}}$ and $\phi_{k \in \text{T, S}}$; hereafter, “states” denote many-electron states and “orbitals” refer to a single-electron energy levels.

The current I_{X} through the molecule/lead contact is given by a sum of contributions from individual orbitals

$$I_{\text{X}}(t) = \sum_{i \in \text{M}} \text{Tr}[J_i^{\text{X}} \rho(t)] \quad \text{X} = \text{T, S} \quad (5)$$

$\rho(t)$ is the time-dependent density matrix of the total system, and J_i^{X} is the current operator for the i th orbital

$$J_i^{\text{X}} = \frac{ie}{\hbar} \sum_{k \in \text{X}} V_{ik} \psi_i^\dagger \psi_k - V_{ki} \psi_k^\dagger \psi_i \quad (6)$$

Upon expanding eq 5 perturbatively in the molecule–lead

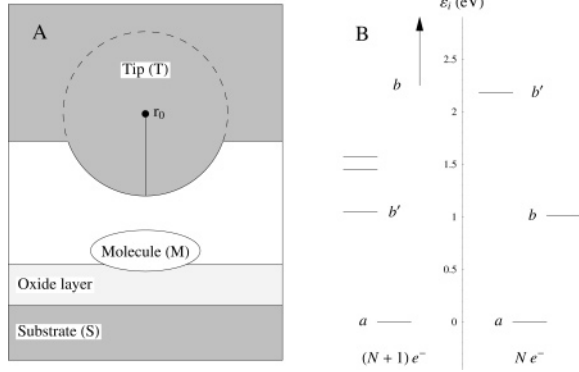


Figure 1. (A) Schematic diagram of the STM junction consisting of the tip, molecule, substrate, and oxide tunneling barrier. (B) Energy level diagram for MgP showing the many electron states of the N and $N + 1$ electron reference configurations. The conductance is enhanced when μ_X is resonant with the energy difference between a and b (or b'), which have one more (or less) electron relative to a ; b and b' may be ground or excited states.

coupling V_{ik} , the second-order contribution can be expressed in terms of nonequilibrium superoperator Green's functions (SGFs) of the molecule and leads¹⁴

$$I_X = \frac{e}{2\pi\hbar} \sum_{ij} \sum_{k \in X} V_{ik} V_{jk} \int dE \times [G_{LR}^{ij}(E) G_{RL}^{lk}(E) - G_{RL}^{ji}(E) G_{LR}^{kl}(E)] \quad (7)$$

where L and R represent “left” and “right” superoperators acting on the ket and bra, respectively, of the density matrix ρ . The first term in eq 7 describes electron transfer to the lead from the molecule, leaving the molecule positively charged, while the second term represents the reverse process, leaving the molecule negatively charged. The energy domain SGFs are related via a Fourier transform to their time domain counterparts

$$G_{\alpha\beta}^{mn}(E) \equiv \int_{-\infty}^{\infty} dt G_{\alpha\beta}^{mn}(t) e^{iEt/\hbar} \quad (8)$$

These can be recast in terms of ordinary (Hilbert space) two-point correlation functions of the Fermi operators

$$G_{LR}^{mn}(t, t') \equiv \frac{i}{\hbar} \text{Tr}[\psi_m^\dagger(t') \psi_n(t) \rho(0)] \quad (9)$$

$$G_{RL}^{mn}(t, t') \equiv \frac{i}{\hbar} \text{Tr}[\psi_m(t) \psi_n^\dagger(t') \rho(0)] \quad (10)$$

Figure 2 shows the double-sided Feynman diagrams for the two SGFs that contribute to the current. G_{LR} represents an electron transfer, while G_{RL} involves hole transfer.

Expanding the molecular Green's functions in many-electron states gives¹⁵

$$G_{LR}^{ij}(t) = \frac{i}{\hbar} \sum_{b'} e^{-iE_{ab'}t} S_{jb',a}^{N-1} S_{ib',a}^N \quad (11)$$

$$G_{RL}^{ji}(t) = \frac{i}{\hbar} \sum_b e^{-iE_{ba}t} S_{ja,b}^{N+1} S_{ib,a}^N \quad (12)$$

where

$$S_{jb',a}^{N-1} \equiv \langle \psi_{j,a} | b' \rangle \quad S_{ib',a}^N \equiv \langle \psi_i^\dagger | b' | a \rangle \quad (13)$$

$$S_{ja,b}^{N+1} \equiv \langle \psi_j^\dagger | a | b \rangle \quad S_{ib,a}^N \equiv \langle \psi_i | b | a \rangle \quad (14)$$

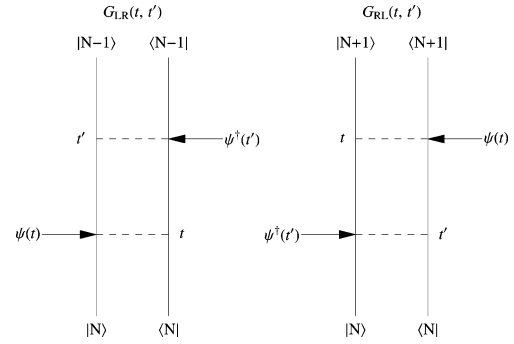


Figure 2. Double-sided Feynman diagrams depicting G_{LR} and G_{RL} . Time moves from bottom to top, and the $|N\rangle \langle N|$ denotes a many-electron density matrix with N electrons. G_{LR} involves the transfer of an electron to the lead from the molecule leaving the molecule positively charged, and G_{RL} represents the transfer of a hole to the lead from the molecule leaving the molecule negatively charged.

are many-body overlap factors; $|a\rangle$, $|b\rangle$, and $|b'\rangle$ refer to the ground state of the neutral molecule (N electrons), the states of the negatively charged molecule ($N + 1$ electrons), and the states of the positively charged molecule ($N - 1$ electrons); $E_{ba} = E_b - E_a$ and $E_{ab'} = E_a - E_{b'}$ are the transition energies; see Figure 1B. In the energy domain, we have

$$G_{LR}^{ij}(E) = 2\pi i \sum_{b'} S_{ja,b'}^{N-1} S_{ib',a}^N \delta(E - E_{ab'}) \quad (15)$$

$$G_{RL}^{ji}(E) = 2\pi i \sum_b S_{ja,b}^{N+1} S_{ib,a}^N \delta(E - E_{ba}) \quad (16)$$

We assume that the leads remain in equilibrium and their grand canonical Green's functions are given by the fluctuation–dissipation relations¹⁶

$$G_{LR}^{kl}(E) = 2\pi i f_X(E) \delta_{kl} \delta(E - \epsilon_k) \quad (17)$$

$$G_{RL}^{lk}(E) = 2\pi i (1 - f_X(E)) \delta_{lk} \delta(E - \epsilon_k) \quad (18)$$

where $f_X(E) = (1 + e^{(E - \mu_X)/kT})^{-1}$ is the Fermi function for lead X with thermal energy kT and chemical potential μ_X . The current dependence on the bias V_b is introduced through the chemical potentials $\mu_T = E_f + \eta e V_b$ and $\mu_S = E_f - (1 - \eta) e V_b$, where E_f is the Fermi energy.¹⁷ The voltage division factor η is related to the potential drop across the junction, which may be controlled by the thickness of the oxide layer. It determines the energy difference between the molecular states and μ_X as V_b is varied.

Inserting eqs 15–18 into eq 7 gives

$$I_X = \sum_b \Gamma_{ba}^X f_X(E_{ba}) - \sum_{b'} \Gamma_{ab'}^X (1 - f_X(E_{ab'})) \quad (19)$$

where

$$\Gamma_{nm}^X = \frac{2\pi e}{\hbar} \sum_{ij \in M} \sum_{k \in X} V_{ik} V_{jk} \delta(E_{nm} - \epsilon_k) S_{jm,n}^{N(n)} S_{in,m}^{N(n)-1} \quad (20)$$

is an effective tunneling rate constant from state m with $N(n) - 1$ electrons to state n with $N(n)$ electrons. Assuming a continuous distribution of the lead energy levels and that its density of states and the coupling to the molecule do not vary over the relevant energy range, we obtain for the tunneling rate constants

$$\Gamma_{nm}^X \propto \frac{2\pi e}{\hbar} \left| \sum_{i \in M} V_i^X S_{im,n}^{N(n)} \right|^2 \quad (21)$$

A similar result was obtained in ref 11 using a kinetic model and master equation approach. These factors follow naturally from the many-body expansion of the molecular Green's functions.¹⁵ The advantage of the Green's function approach is that all interactions and coherence effects can be included exactly through self-energies. The master equation approach is simpler to interpret but requires further approximations to achieve closure; coherence effects are usually ignored. The present description avoids the self-energy calculation by formulating the problem directly in terms of the many-body states for the neutral and charged molecule and by the weak coupling assumption to the leads.

In our simulations we treat states *a*, *b*, and *b'* at the Hartree–Fock (HF) and configuration interaction singles (CIS) level¹⁸ where the ground electronic state (a single Slater determinant) is used as the reference for constructing the excited states in terms of singly excited Slater determinants. The nuclear geometry of the molecule for the states *a*, *b*, and *b'* is constrained to the equilibrium geometry for our reference state *|a⟩*. This assumption is justified if the electron tunneling rates are faster than the response of the nuclear degrees of freedom to the additional charge. One could relax this restriction by considering a complete set of vibronic states for the $N \pm 1$ states of the molecule. These consist of both electronic and vibrational components and would need to be calculated at different nuclear configurations; however, this goes beyond the present study.

Let *|A⟩*, *|B⟩*, and *|B'⟩* denote to the ground-state Slater determinants constructed from the relaxed molecular orbitals of the N , $N + 1$, and $N - 1$ electron molecules

$$|A\rangle = N!^{-1/2} \det\{\phi_1^A \dots \phi_N^A\} \quad (22)$$

$$|B\rangle = (N + 1)!^{-1/2} \det\{\phi_1^B \dots \phi_{N+1}^B\} \quad (23)$$

$$|B'\rangle = (N - 1)!^{-1/2} \det\{\phi_1^{B'} \dots \phi_{N+1}^{B'}\} \quad (24)$$

Here, each column of the Slater determinant is represented by the diagonal element ϕ_i corresponding to electron *i* occupying the *i*th molecular orbital. Note that the relaxed orbitals of the charged molecule are not orthogonal to those of the neutral molecule; hence, one cannot construct *|B⟩* by simply adding a column and row to *|A⟩*. For $N + 1$ electrons, the excited states are given by $|b\rangle = \sum_{ij} c_{ij}^b |B_i^b\rangle$ where c_{ij}^b is the CIS coefficient for the singly excited Slater determinant $|B_i^b\rangle$ constructed by transferring an electron from the occupied ϕ_i to a virtual ϕ_j

$$|B_i^b\rangle = (N + 1)!^{-1/2} \times \det\{\phi_1^B \dots \phi_{i-1}^B \phi_j^B \phi_{i+1}^B \dots \phi_{N+1}^B\} \quad (25)$$

Similarly, the Slater determinants $|A_i\rangle = |\psi_i A\rangle$ and $|A^i\rangle = |\psi_i^\dagger A\rangle$ are constructed from the molecular orbitals of the reference state by adding a hole or electron, respectively, in ϕ_i to *|A⟩*

$$|A_i\rangle = (-1)^{i-1} N!^{-1/2} \det\{\phi_1^A \dots \phi_{i-1}^A \phi_{i+1}^A \dots \phi_N^A\} \quad (26)$$

$$|A^i\rangle = (-1)^N N!^{-1/2} \det\{\phi_1^A \dots \phi_N^A \phi_i^A\} \quad (27)$$

The many-body overlap factors of Slater determinants containing $N + 1$ and $N - 1$ electrons, respectively, are then written as

$$S_{ia,b}^{N+1} = \sum_{jk} c_{jk}^b \langle A_i^i | B_j^b \rangle \quad (28)$$

$$S_{ia,b'}^{N-1} = \sum_{jk} c_{jk}^{b'} \langle A_i^i | B_j^{b'} \rangle \quad (29)$$

The overlap of two Slater determinants *|P⟩* and *|Q⟩* is given by the determinant of a matrix $\langle P|Q\rangle = \det\{S\}$ whose elements $S_{ij} = \langle \phi_i^P | \phi_j^Q \rangle$ are the overlap integrals between occupied orbitals.¹⁹ As noted earlier, these electronic overlaps are calculated between states with the same nuclear configuration (vertical transitions). In order to include the effects of nuclear relaxation upon charging, one could introduce a set of Franck–Condon factors describing the overlap of nonorthogonal vibrational wave functions between the different charge states N and $N \pm 1$.

The spatial dependence of the current is determined by the variation of the coupling V_i^T with the position of the STM tip.²⁰ The tip is represented by a spherical orbital $|r_T\rangle$ centered at r_T ; the coupling is assumed to be proportional to the overlap $V_i^T \propto \langle \phi_i | r_T \rangle$.²¹

Results and Discussion

We have calculated the STM conductance spectrum of the neutral and charged states of MgP at the tip–molecule contact. This involves a series of electronic structure calculations to determine the electronic states of neutral and anionic MgP, the many-body overlap factors, and the molecule–tip coupling. To calculate the conductance using eq 19, we set the Fermi energy E_f to zero and use η as an adjustable parameter to fit the experimental conductance.²²

The electronic structure calculations are described below.²³ First, a pair of reference configurations for the neutral and anionic MgP are found by minimizing the ground-state energy with respect to the molecular geometry using the unrestricted Hartree–Fock (UHF) method with a 3-21G basis set. The neutral equilibrium geometry is used to calculate the electronic states involved in the conductance of the neutral molecule, and the anion equilibrium geometry is used to calculate the electronic states involved in the conductance through the anion.

In the experimental setup,⁶ MgP is adsorbed on an ultrathin aluminum oxide layer grown on a NiAl(110) surface. The effects of the oxide layer are included approximately by treating it as a static charge distribution. To determine an appropriate set of point charges, we have made use of calculations reported by Kresse and co-workers in which the unit cell geometry has been determined via plane wave density functional theory (DFT).²⁴ We performed a single point DFT energy calculation of the oxide unit cell under periodic boundary conditions using the PBE exchange–correlation functionals with a 3-21G basis. A Mulliken population analysis of the ground-state density matrix was used to assign partial charges to the oxide atoms; a 3×3 supercell of alumina charges was then constructed and included into the electronic structure calculations of MgP. The configuration of the alumina charges was frozen in our calculations. In general, the aluminum and oxygen atoms would respond to the charge state of the MgP adsorbate; however, we ignored this effect and used a fixed configuration in the interest of simplicity.

A suitable binding configuration for the MgP was obtained by minimizing the UHF/3-21G energy with respect to translating and spinning the molecule in a fixed plane parallel to the charges

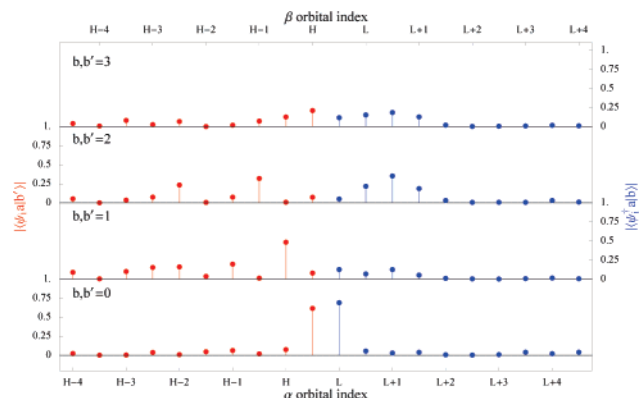


Figure 3. Many-body overlap factors between the N electron ground state $|\alpha\rangle$ of MgP and the four lowest energy states $|b'\rangle$ and $|b\rangle$ with $N - 1$ and $N + 1$ electrons, respectively. The horizontal axes indicate the orbital where the hole or electron is created. Results are given for (red) hole injection into the highest ten occupied and (blue) electron injection into the lowest ten unoccupied spin orbitals; the upper and lower horizontal axes index the up α and down β spin orbitals, respectively. The low-energy conductance peaks involving the ground states of the charged molecule are dominated by the contribution from the HOMO and LUMO. The higher energy peaks which involve the excited states of the charged molecule contain more or less equal contributions from different orbitals.

at a height of 2 Å above the uppermost layer of the oxide structure; the same binding configuration was used for the anionic MgP. Note that the internal nuclear degrees of freedom of the molecule were constrained to the vacuum equilibrium positions even in the presence of the charge distribution, and only the electronic structure was allowed to relax. The ground-state electronic energies, atomic overlap integrals, and molecular coefficients of both the neutral and anionic equilibrium geometries were stored for later use. Next, the electronic states of the $N + 1$ and $N - 1$ electron species were calculated at the neutral MgP reference geometry at the unrestricted CIS level with a 3-21G basis set. The electronic state energies, molecular orbital coefficients, and CIS coefficients were stored. A similar calculation was performed for the anionic reference geometry, however, these calculations involved the N electron and $N + 2$ electron states. Finally, we calculated the one-electron overlap integrals between the atomic basis of the reference geometries and a 51×51 grid of spherical Gaussian tip orbitals (width $\sigma = 2$ Å) positioned 3 Å above and parallel to the molecular plane of MgP.

We assembled the tunneling rate constants and the current using the stored output from the quantum chemistry calculations for both the neutral and anionic reference systems. The tunneling elements $V_i^T(r_T)$ at each tip position were calculated using the reference state's molecular orbital coefficients and the tip–molecule atomic overlap matrix. For both $N + 1$ and $N - 1$ electronic configurations at the neutral reference geometry, we used the atomic overlap integrals and the orbital coefficients to construct a pair of master overlap matrices between the orbitals of the neutral and charged molecules. We then constructed the various occupied–occupied overlap matrices whose matrix determinants give the different terms which are summed in eq 21. The number of matrix determinants is truncated by retaining terms whose CIS coefficients are greater than 0.1. With the tunneling rate constants Γ_{ab} and $\Gamma_{b'a}$, the current and conductance are evaluated according to eq 19.

In Figure 3, we compare the many-body overlap factors between the ground state of the neutral MgP and the four lowest energy states of $N \pm 1$ electron MgP. The points along the horizontal axis indicate the orbital where the electron is created

or annihilated. The tunneling rate constants for the ground states are dominated by the terms corresponding to an electron annihilated from the highest occupied or created in the lowest unoccupied orbitals. This is not the case for the rate constants involving the excited charged states, where there are comparable contributions from several different orbitals. The many-body rather than single-electron (orbital) theory is then required.

Experimentally, MgP is observed to switch between two states with different conductance profiles (dI/dV versus V curves); the evidence given in ref 6 suggests that the two states exhibit a difference in charge and were identified as the neutral and anionic ground states. The actual identity of the charged states may not be determined solely from the empirical data. Our simulations show that the cation and double-charged anionic states are at much higher energies (see Figure 1B). This agrees with the identification of the charge states proposed in ref 6.

The neutral MgP conductance is negligible between -1.5 and 0.55 V where the onset of a peak is observed. Since there is no $\pm V$ symmetry in the conductance and our calculations predict that $|E_{ab}| > 2.0$ eV, then η must be nearly equal to 1. This can be rationalized by considering the fact that the oxide thickness is greater than 5 Å so that the tip–molecule distance may be shorter than the tip–substrate distance. The experimental conductance spectrum for anionic MgP exhibits a slight symmetry with the onset of low-intensity peaks at -0.45 and 0.7 V. The potential drop across the junction should be affected by the additional charge on the molecule; the symmetry of the conductance spectra and the fact that $|E_{ba}|$ is much larger than $|E_{ab}|$ implies $\eta \approx 1/2$ and that the observed peaks for the negatively charged MgP are due to bipolar conduction involving the N electron states. Using different η values for the neutral and anionic MgP may be justified based on the experimental observation that the STM tip retracts when MgP is charged so that the tip–molecule and the molecule–substrate distances may become comparable.

In Figure 4, we show the calculated conductance spectra for (A) the neutral and (B) the negatively charged reference configurations of MgP at the ten tip positions indicated in panel a. The asymmetry (symmetry) of the conductance spectra for the neutral (anionic) reference configurations comes from the η values used. Panels a–d show the spatially resolved conductance maps (at fixed bias) for the correspondingly labeled peaks in panels A and B. Panels a and b show the spatial distribution of the conductance through the $N - 1$ and $N + 1$ electron ground states at the neutral MgP reference configuration. Panels c and d depict the spatially resolved conductance maps of the ground and lowest excited N electron states at the anionic reference geometry. The same states give rise to symmetric peaks at negative bias. The $N + 2$ electronic states have much higher energies and are beyond this range of bias values. The asymmetric patterns in the stimulated conductance maps reflect the distortions induced by the underlying alumina charge distribution. The calculated conductance maps show an enhancement on the outer rings of the MgP and a diminished conductance over the central Mg atom; this is consistent with the experimental STM images, especially for peak b where the calculated map reproduces the observed characteristic ten-lobe pattern.

In summary, we have combined a many-body expansion of the molecular Green's function with electronic structure calculations to simulate the conductance spectra for different charge states of a single MgP molecule in a STM junction. The conductance is calculated by employing a sum-over-states

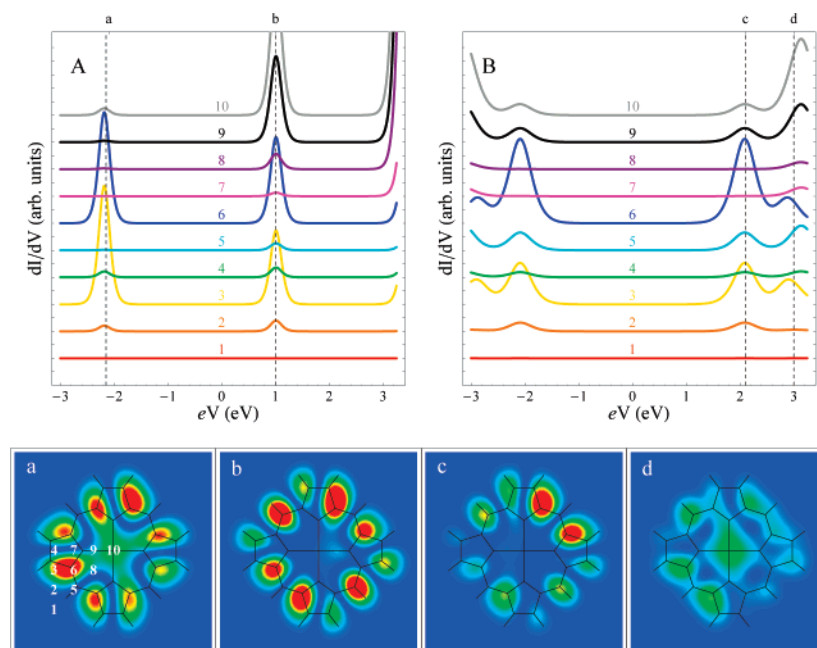


Figure 4. Calculated STM conductance spectra for (A) the neutral magnesium porphyrine (MgP) reference configuration with $\eta = 1$ (asymmetric spectra) and (B) the negatively charged MgP reference configuration with $\eta = 0.5$ (symmetric spectra). The curves labeled 1–10 are displaced vertically for clarity and correspond to the different lateral tip positions indicated by the white numbers in panel a. Panels a–d are the spatially resolved dI/dV signals for the four peaks marked with dashed lines in panels A and B. Peaks a and b are due to tunneling through ground electronic states of the $N - 1$ and $N + 1$ electronic ground states, respectively, at the neutral MgP geometry. Peaks c and d are due to tunneling through the ground state of the N electronic ground and the first excited states, respectively, at the negatively charged MgP geometry. These peaks also occur at negative bias and have identical spatial profiles.

expression which shows peaks when the chemical potential of the tip becomes resonant with the energy difference between the N electron reference state and the $N \pm 1$ ground or excited states. The peak intensities are determined by a set of tunneling rate constants which involve the squared sum of many-body overlap factors corresponding to charge transfer to each of the molecular orbitals. The differences in the experimental conductance spectra of neutral and charged states of MgP can be attributed to the different voltage division across the STM junction.

Acknowledgment. We wish to thank George V. Nazin, Dr. Shiwei Wu, and Professor Wilson Ho for useful discussions. The support of the National Science Foundation (CHE-0446555, NIRT EEC-0406750, and CBC CHE-0533162) is gratefully acknowledged.

References and Notes

- (1) Mannik, J.; Goldsmith, B. R.; Kane, A.; Collins, P. G. *Phys. Rev. Lett.* **2006**, *97*, 016601.
- (2) Chen, J.; Reed, M. A. *Chem. Phys.* **2002**, *281*, 127.
- (3) (a) Keane, Z. K.; Ciszek, J. W.; Tour, J. M.; Natelson, D. *Nano Lett.* **2006**, *6*, 1518. (b) Danilov, A. V.; Kubatkin, S. E.; Kafanov, S. G.; Flensberg, K.; Bjornholm, T. *Nano Lett.* **2006**, *6*, 2184.
- (4) (a) DeLonno, E.; Tseng, H.-R.; Harvey, D. D.; Stoddart, J. F.; Heath, J. R. *J. Phys. Chem. B* **2006**, *110*, 7609. (b) Flood, A. H.; Wong, E. W.; Stoddart, J. F. *Chem. Phys.* **2006**, *324*, 280.
- (5) Choi, B.-Y.; Kahng, S.-J.; Kim, S.; Kim, H.; Kim, H. W.; Song, Y. J.; Ihm, J.; Kuk, Y. *Phys. Rev. Lett.* **2006**, *96*, 156106.
- (6) Wu, S. W.; Ogawa, N.; Ho, W. *Science* **2006**, *312*, 1362.
- (7) Wu, S.; Nazin, G.; Chen, X.; Qiu, X. H.; Ho, W. *Phys. Rev. Lett.* **2004**, *93*, 236802.
- (8) (a) Qiu, X. H.; Nazin, G.; Ho, W. *Phys. Rev. Lett.* **2004**, *92*, 206102. (b) Lee, H. J.; Lee, J. H.; Ho, W. *ChemPhysChem* **2005**, *6*, 971. (c) Nazin, G. V.; Wu, S. W.; Ho, W. *Proc. Natl. Acad. Sci. U.S.A.* **2005**, *102*, 8832.
- (9) Qiu, X. H.; Nazin, G. V.; Ho, W. *Science* **2003**, *299*, 542.
- (10) (a) Dong, Z.-C.; Guo, X.-L.; Trifonov, A. S.; Dorozhkin, P. S.; Miki, K.; Kimura, K.; Yokoyama, S.; Mashiko, S. *Phys. Rev. Lett.* **2004**, *92*, 086801. (b) Guo, X.-L.; Dong, Z.-C.; Trifonov, A. S.; Miki, K.; Wakayama, Y.; Fujita, D.; Kimura, K.; Yokoyama, S.; Mashiko, S. *Phys. Rev. B* **2004**, *70*, 233204. (c) Guo, X.-L.; Dong, Z.-C.; Trifonov, A. S.; Miki, K.; Mashiko, S.; Okamoto, T. *Nanotechnology* **2004**, *14*, S402. (d) Guo, X.-L.; Dong, Z.-C.; Trifonov, A. S.; Yokoyama, S.; Mashiko, S.; Okamoto, T. *Appl. Phys. Lett.* **2004**, *84*, 979. (e) Guo, X.-L.; Dong, Z.-C.; Trifonov, A.; Miki, K.; Kimura, K.; Mashiko, S. *Appl. Surf. Sci.* **2005**, *241*, 28. (f) Guo, X.-L.; Dong, Z.-C.; Trifonov, A. S.; Miki, K.; Kimura, K.; Mashiko, S. *Appl. Phys. A* **2005**, *81*, 367. (g) Liu, H.; Je, Y.; Yoshinobu, T.; Aso, Y.; Iwasaki, H. *Appl. Phys. Lett.* **2006**, *88*, 061901.
- (11) Muralidharan, B.; Ghosh, A. W.; Datta, S. *Phys. Rev. B* **2006**, *73*, 155410.
- (12) (a) Karzazi, Y.; Cornil, J.; Brédas, J. L. *J. Am. Chem. Soc.* **2001**, *123*, 10076. (b) Karzazi, Y.; Cornil, J.; Brédas, J. L. *Nanotechnology* **2003**, *14*, 165. (c) Liu, R.; Ke, S.-H.; Baranger, H. U.; Yang, W. *J. Am. Chem. Soc.* **2006**, *128*, 6274.
- (13) (a) Gaudioso, J.; Lauhon, L. J.; Ho, W. *Phys. Rev. Lett.* **2000**, *85*, 1918. (b) Qiu, X. H.; Nazin, G. V. *Phys. Rev. Lett.* **2004**, *93*, 196806. (c) Galperin, M.; Ratner, M. A.; Nitzan, A. *Nano Lett.* **2005**, *5*, 125.
- (14) Harbola, U.; Maddox, J. B.; Mukamel, S. *Phys. Rev. B* **2006**, *73*, 205404.
- (15) Harbola, U.; Maddox, J. B.; Mukamel, S. *Phys. Rev. B* **2006**, *73*, 075211.
- (16) (a) Caroli, C.; Combescot, R.; Nozieres, P.; Saint-James, D. *J. Phys. C: Solid State Phys.* **1972**, *5*, 21. (b) Haug, H.; Jauho, A.-P. *Quantum Kinetics in Transport and Optics of Semiconductors*; Springer: Germany, 1996.
- (17) Datta, S.; Tian, W.; Hong, S.; Reifenberger, R.; Henderson, J. I.; Kubiak, C. P. *Phys. Rev. Lett.* **1997**, *79*, 2530.
- (18) (a) Szabo, A.; Ostlund, N. S. *Modern Quantum Chemistry, Introduction to Advanced Electronic Structure Theory*; McGraw-Hill: New York, 1989. (b) Foresman, J. B.; Head-Gordon, M.; Pople, J. A.; Frisch, M. J. *J. Phys. Chem.* **1992**, *96*, 135.
- (19) Campbell, L.; Mukamel, S. *J. Chem. Phys.* **2004**, *121*, 12323.
- (20) (a) Tersoff, J.; Hamann, D. R. *Phys. Rev. Lett.* **1983**, *50*, 1998. (b) Tersoff, J.; Hamann, D. R. *Phys. Rev. B* **1985**, *31*, 805. (c) Bardeen, J. *Phys. Rev. Lett.* **1961**, *6*, 57.
- (21) The coupling element should be calculated according to Bardeen's formula;²⁰ however, we adopt a more approximate approach and take it to be simply proportional to an overlap.
- (22) The experimental conductance curves for MgP are described as follows: see ref 6. In the neutral state, the MgP molecule exhibits negligible conductance in the bias range of -1.5 – 0.55 V. Beyond 0.55 V, the conductance increases smoothly but then sharply drops around 0.85 V; the sudden drop is attributed to the MgP accepting an extra electron. As the bias is scanned further, an additional peak at 1.5 V is found. Evidence that MgP is charged is found when the bias is scanned in the reverse direction,

and the onset of the first peak is shifted up by 0.15 V, and the conductance is dramatically reduced. At negative values, the conductance begins to smoothly increase around -0.45 V (this peak is not observed for the neutral charge state) but then sharply drops to 0 at around -1.0 V; this is attributed to a discharging event. No peaks are observed at larger negative bias values down to -1.5 V. The charging/discharging cycle can be performed repeatedly such that statistics can be made on the threshold bias required for charging/discharging to occur. Additionally, the threshold bias required to switch from one charge state to the other is effected by the frequency and intensity of a CW laser field and the position of the STM tip.

(23) (a) All of the quantum chemistry calculations reported here are performed with the Gaussian 03 package. Frisch, M. J.; Trucks, G. W.; Schlegel, H. B.; Scuseria, G. E.; Robb, M. A.; Cheeseman, J. R.; Montgomery, J. A., Jr.; Vreven, T.; Kudin, K. N.; Burant, J. C.; Millam, J. M.; Iyengar, S. S.; Tomasi, J.; Barone, V.; Mennucci, B.; Cossi, M.; Scalmani, G.; Rega, N.; Petersson, G. A.; Nakatsuji, H.; Hada, M.; Ehara,

M.; Toyota, K.; Fukuda, R.; Hasegawa, J.; Ishida, M.; Nakajima, T.; Honda, Y.; Kitao, O.; Nakai, H.; Klene, M.; Li, X.; Knox, J. E.; Hratchian, H. P.; Cross, J. B.; Bakken, V.; Adamo, C.; Jaramillo, J.; Gomperts, R.; Stratmann, R. E.; Yazyev, O.; Austin, A. J.; Cammi, R.; Pomelli, C.; Ochterski, J. W.; Ayala, P. Y.; Morokuma, K.; Voth, G. A.; Salvador, P.; Dannenberg, J. J.; Zakrzewski, V. G.; Dapprich, S.; Daniels, A. D.; Strain, M. C.; Farkas, O.; Malick, D. K.; Rabuck, A. D.; Raghavachari, K.; Foresman, J. B.; Ortiz, J. V.; Cui, Q.; Baboul, A. G.; Clifford, S.; Cioslowski, J.; Stefanov, B. B.; Liu, G.; Liashenko, A.; Piskorz, P.; Komaromi, I.; Martin, R. L.; Fox, D. J.; Keith, T.; Al-Laham, M. A.; Peng, C. Y.; Nanayakkara, A.; Challacombe, M.; Gill, P. M. W.; Johnson, B.; Chen, W.; Wong, M. W.; Gonzalez, C.; Pople, J. A. *Gaussian 03*, revision C.02; Gaussian, Inc.: Wallingford, CT, 2004. (b) We have also made use of computational results reported by Kresse and co-workers; see the computational details section of the supporting information and ref 24 for more details.

(24) Kresse, G.; Schmid, M.; Napetschnig, E.; Shishkin, M.; Köhler, L.; Varga, P. *Science* **2005**, 308, 1440.